

He I 10830 Å LINE POLARIMETRY: A NEW TOOL TO PROBE THE FILAMENT MAGNETIC FIELDS

HAOSHENG LIN

National Solar Observatory/Sacramento Peak, P.O. Box 62, Sunspot, NM 88349; lin@sunspot.noao.edu

MATT J. PENN

National Solar Observatory/Tucson, P.O. Box 26732, Tucson, AZ 85726-6732

AND

JEFFREY R. KUHN

National Solar Observatory/Sacramento Peak, P.O. Box 62, Sunspot, NM 88349, and Michigan State University, East Lansing, MI 48824

Received 1996 September 27; accepted 1997 September 4

ABSTRACT

In this paper, we present a new Stokes polarization observation of a solar filament using the neutral helium line at 10830 Å. Similar to the prominence Hanle effect, the polarization of the filament is due to the resonant scattering and magnetic depolarization of the photospheric radiation; it differs only in the scattering geometry. Since this represents one of the first filament polarization observations, we also present a classical derivation of a set of diagnostic formulae that relate the filament polarization signals to the vector magnetic field.

We measured the full Stokes profiles (I , Q , U , V) by scanning the slit of the spectrograph parallel to the axis of a small filament. In one section of the filament, the polarization signals showed that the axial component of the magnetic field reverses direction on either side of the filament axis. This axial field reversal is not predicted by any of the existing magnetic field models of the filament, nor was it observed by previous prominence Hanle effect observations. We propose that a tilted magnetic field loop across the filament axis can explain the observed axial field reversal.

This observation also serves to demonstrate that measurements of the polarization of the He I 10830 Å radiation from filaments is a useful new tool for the diagnostics of filament magnetic field structures.

Subject headings: instrumentation: polarimeters — polarization — Sun: filaments — Sun: infrared — Sun: magnetic fields

1. INTRODUCTION

Most of our knowledge of the filament magnetic fields is derived from direct prominence polarization observations using the Hanle effect (consult the review by Leroy 1989 for a summary) or indirectly from studies of the filament fine structures from H α images (Anzeer & Tandberg-Hanssen 1970; Rust & Kumar 1994; Martin, Bilimoria, & Tracadas 1994). Polarization observations of prominences were mostly done in the He I D₃ line at 5878 Å (Leroy 1989). Leroy, Bommier, & Sahal-Br  chot (1984) and Bommier et al. (1994) also used simultaneous H α and He I D₃ polarimetry to study the vector magnetic fields of prominences. However, filaments do not show strong absorption on the solar disk at the wavelength of He I D₃. Thus, polarization measurements of filaments against the solar disk were difficult, and He I D₃ observations have been limited to limb prominence observations.

Similar to the H α line, filaments also appear as dark absorption features at the He I 10830 Å wavelength. The line absorption of the He I 10830 Å line is generally believed to be due to the resonance scattering redistribution of the photospheric radiation by the neutral helium in the filament. Because the strong He I 10830 Å line is in the near infrared, only recent advancements in infrared array technology have made it possible to measure the polarization of the He I 10830 Å radiation from a filament against the solar disk.

The polarization of the solar radiation could arise from several mechanisms. The most well known are the longitu-

dinal and transverse Zeeman effects used for the magnetic field diagnostics of photospheric magnetic features like sunspots, faculae, and intranetwork magnetic fields. Another polarization mechanism is the Hanle effect, used mostly for diagnostics of solar prominence magnetic fields (Leroy 1989) and turbulent photospheric magnetic fields (Stenflo 1982). The Hanle effect is fundamentally a coherence phenomenon that can only occur when coherent scattering contributes to the formation of the spectral line. In contrast, the usual Zeeman effect polarization does not require scattering, but the Zeeman substates can be uncorrelated with each other, as they are in the case of collisional excitation. It is the nonscattering Zeeman effect that is generally used for observations with solar magnetographs.

Scattering of unpolarized incident radiation produces linear polarization, and a magnetic field modifies this polarization via the Hanle effect by depolarizing it and rotating its direction. A line-of-sight magnetic field can also generate circular polarization by the longitudinal Zeeman effect, which occurs (with different contributions), both when the excitation is by radiation (as in scattering) and by collisions. While the field-strength sensitivity to the Hanle effect (in the linear polarization) depends on the ratio between the Zeeman splitting and the natural width of the excited state, the longitudinal Zeeman effect (the circular polarization) depends on the ratio between the Zeeman splitting and the Doppler width. The Hanle effect is therefore sensitive to much weaker magnetic fields than the usual Zeeman effect (Stenflo 1994).

In the present paper we apply for the first time the Hanle effect to polarimetric observations of filaments against the solar disk. As the linear-polarization Hanle effect is insensitive to vertical magnetic fields when the illumination of the scattering particles is axisymmetric, it only provides information in the horizontal plane of a prominence, regardless of whether it is observed at the limb or against the disk. When observing prominence at the limb, the line of sight lies in the horizontal plane, so the longitudinal Zeeman effect is also insensitive to vertical magnetic fields. This situation is, of course, different for filaments on the disk, for which Stokes V observations may complement the Hanle diagnostics to obtain the full vector magnetic field.

One goal of this paper is to develop a diagnostic tool that can be used for the interpretation of the filament polarization observations. We will formulate the magnetic scattering problem within the context of classical electrodynamics only. We will assume that scattering is the primary source of the observed polarization signals, and that the scattering atmosphere is optically thin, and will consider only the single scattering process. This approach has the advantage that it gives a simple and clear physical picture of the interaction between the magnetic field and the polarization states of the scattered radiation, without the complication of a full quantum mechanical treatment. The result of this formulation is a set of formulae that directly relate the observed Stokes polarization signals to the vector magnetic field of the filament. For a complete treatment of the Hanle effect, including both classical and quantum mechanical derivation, the readers are referred to the monograph of Stenflo (1994).

The validity of the assumption that scattering is the primary polarization mechanism of the He I 10830 Å line radiation requires more careful examination since there may be other sources of emission in addition to the scattering of the photospheric radiation. The He I 10830 Å line results from the transition between the 2^3P and 2^3S states of the orthohelium atoms. It had long been established that the orthohelium in the solar atmosphere is populated by the ionization of He I atoms from the coronal UV and X-ray radiation followed by recombination (Hirayama 1971; Zirin 1975). At the chromospheric level, collisional excitation from the 1^1S to 2^3S state may also contribute to the formation of the orthohelium (Milkey, Heasley, & Beebe 1973). However, due to the low observed electron density in prominences ($n_e \approx 10^{10}$ to 10^{11} cm $^{-3}$; Tandberg-Hanssen 1974; Chang & Deming 1997), the orthohelium in the filament may be primarily formed by the ionization-recombination processes if they are formed locally. Since all the cascading downward transitions following the recombination eventually lead to the 2^3P to 2^3S transition, the ionization-recombination processes may also have a significant contribution to the observed He I 10830 Å line emission. Because the ionization-recombination process is incoherent, the polarization should be described by the Zeeman effect. Another mechanism to populate the 2^3P level that results in Zeeman effect polarization signals is collisional excitation. But we can safely dismiss this possibility due to the low electron density.

In the weak magnetic field regime we expected in the filament environment, the Zeeman effect does not contribute significantly to the linear polarizations. In the circulation polarization measurement, however, both Zeeman effect and Hanle effect may contribute. The relative impor-

tance of the Zeeman effect polarization in the Stokes V observation depends on the efficiency of the He I ionization process. The fact that filaments appear as dark absorption features against the solar disk suggests that coherence scattering should have important contribution to the polarization signals of the filaments. The shape of the linear polarization line profiles we observed also show strong signatures of scattering polarization. Therefore, Hanle effect should have strong contribution to the observed polarization signals. Unfortunately, we do not have an estimate on the relative strength of the emission due to the ionization-recombination process. We cannot estimate the contribution of the Zeeman effect circular polarization. Since the Zeeman effect polarization mechanism is well known, we will only concentrate in deriving the Stokes profiles caused by the Hanle effect in this paper.

Bearing in mind the preliminary nature of this experiment and our goal to develop a simple and understandable diagnostic tool for the observational data, we do acknowledge that a full quantum mechanical treatment for the magnetic scattering of the He I 10830 Å line is needed for a more accurate quantitative analysis of the observational data.

2. THE STOKES OBSERVATIONS AND THE DATA SET

The instrumentation of this experiment is similar to that reported in Lin (1995), except that two new liquid crystal variable retarders (LCVR) with faster transition time were integrated into the system. The first LCVR is placed immediately after the slit of the spectrograph with its fast axis rotated 90° with respect to the direction of the slit. A second LCVR with its fast axis rotated 45° with respect to the slit is placed behind the first LCVR. It is followed by a linear polarizer aligned with the slit direction. This setup allowed us to analyze the complete Stokes vector. The observation cycles through the three Stokes polarization states (Q , U , V) sequentially. For each polarization state, the LCVRs switch between two retardations measuring the two opposite polarization intensities (e.g., $I + Q$ and $I - Q$) at a frequency of about 4 Hz. To achieve high signal-to-noise ratio, we integrated 160 pairs of the orthogonal states for each Stokes profile. The large integration number also reduces spurious seeing signals. In addition, a correlation tracker was used to reduce the image motions during the scan.

We obtained this filament observation on 1995 October 21. The filament we observed was located at 40° north, and 8° west on the solar disk. The length of the filament was approximately 80". The Sac Peak H α flare patrol images suggest that it is formed in a long, mostly empty filament channel. It is also rapidly evolving, changing shape from one day to the next (Fig. 1). The direction of the first part of its axis (labeled section A in Fig. 1) is aligned with the local solar radius vector direction. The projection of the second part of the axis (labeled section B) of the filament bends toward the west, making approximately a 20° angle with the axis of section A. We placed the slit roughly perpendicular to the axis of section B, and scanned the area with 40 steps of 2" each. In this slit orientation, the angle between the x direction on the optical bench (for which the Stokes Q is defined) and the direction of the local solar limb is 40°. Thus, the observed Stokes Q and U profiles were rotated such that the Stokes Q measures the linear polarization along the local solar limb. The Stokes profile images of the eighth scan step (position $x = 16''$ Fig. 5 below) are shown

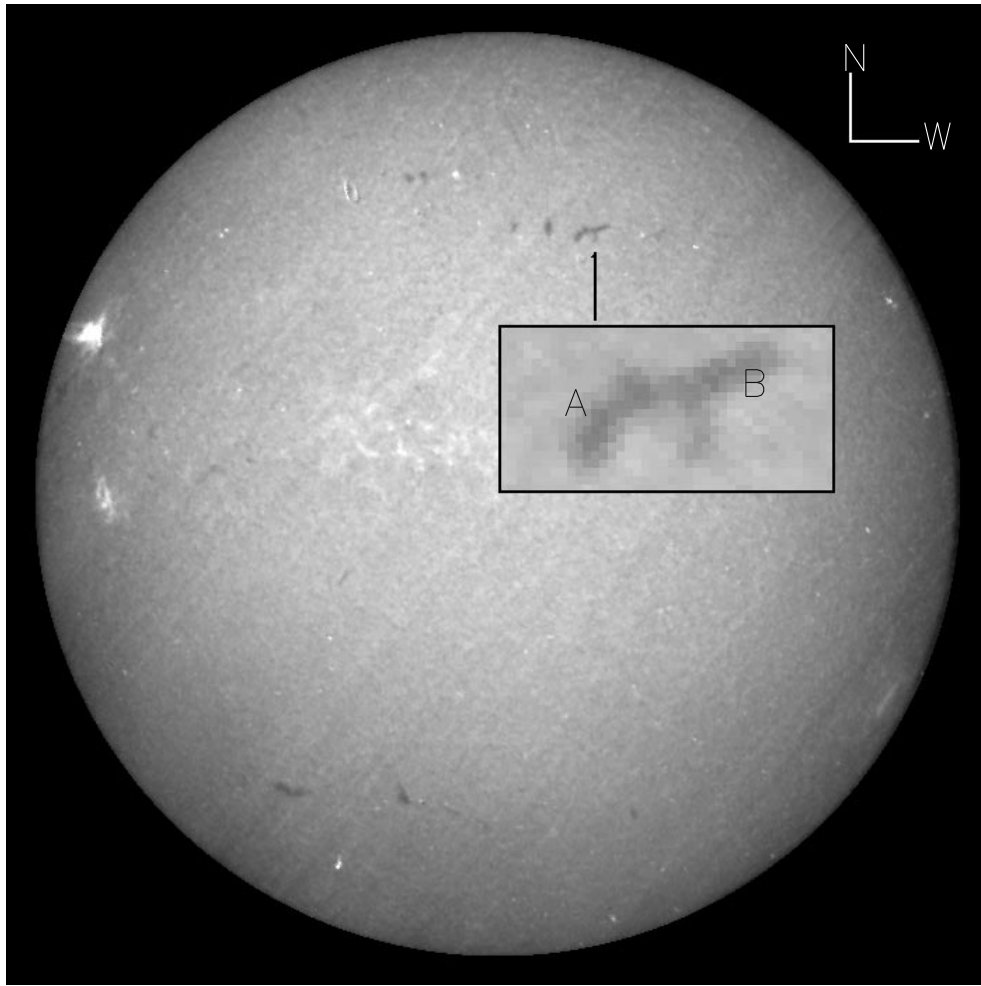


FIG. 1.—Sacramento Peak full-disk $H\alpha$ flare patrol image of the filament. The insert is an enlarged picture of the filament we observed.

in Figure 2. Our spectral window covers both the He I 10830 Å and the Si I 10827 Å line. The Si I 10827 Å line is formed in the photosphere and has weak magnetic sensitivity with a Lande factor of $g = 1.5$. It is used as a simultaneous measurement of the photospheric magnetic field.

Line plots of the four Stokes profiles from slit position $y = 42''$ of the Stokes profile images in Figure 2 are shown in Figure 3. The amplitude of the Stokes I absorption is about 15%. The amplitude of the Stokes Q and U are approximately 2% of the continuum intensity. The noise is at 0.1% continuum intensity level. The Stokes Q and U profiles are similar in shape to the Stokes I profile. This is consistent with previous prominence Hanle effects observations (Landi Degl'innocenti 1982). We did not detect any significant Stokes V signal in the He I 10830 Å line throughout the scan. This is also consistent with previous prominence observations which showed that the Stokes V signal in prominences is typically 1 order of magnitude smaller than the Q and U signal (Landi Degl'innocenti 1982). From the amplitude of the Stokes Q and U signal, the expected Stokes V amplitude is at the order 0.1%, which is close to our noise level. Thus, it is not surprising that we did not register strong circular polarization from the filament.

The vacuum tower telescope of Sacramento peak is known to have strong polarization cross-talk between the Stokes V and U state at the 1.6 μm wavelength (Kuhn et al. 1994). However, because of a fortuitous compensating tele-

scope optics configuration, the cross talk at 1.1 μm is weak. Figure 4 shows the Stokes profile images obtained across a sunspot umbra at He I 10830 Å and Si I 10827 Å wavelengths just before the filament scan without cross talk correction. It is clear from these images that the cross talk between the polarization states is small since the Stokes Q and U profiles are approximately symmetric with respect to the line center, and the Stokes V is antisymmetric without a central component. We applied the cross talk correction technique described in Kuhn et al. using the Si I 10827 Å line and found a maximum cross talk coefficient of about 5%. Because of the intrinsically weak Stokes V polarization of these data, we can safely use the uncorrected polarization measurements of the He I 10830 Å line even when no sunspot is available for cross talk calibration measurement.

House (1971) showed that in Hanle effects the degree of polarization along the line profile is the same (broadband polarimetric measurements without resolving the spectral profile are sufficient to infer the magnetic field structure of the prominence). Therefore we can construct a polarization map of the filament by integrating over the line profile. Figure 5 shows the integrated Stokes I , Q , U maps of the He I 10830 Å line, and the photospheric magnetogram obtained from the Stokes V profiles of the Si I 10827 Å line. At 0.1% noise level, the Si I magnetogram does not have the sensitivity to show the intranetwork fields, although it does show that at the photospheric level, the network elements

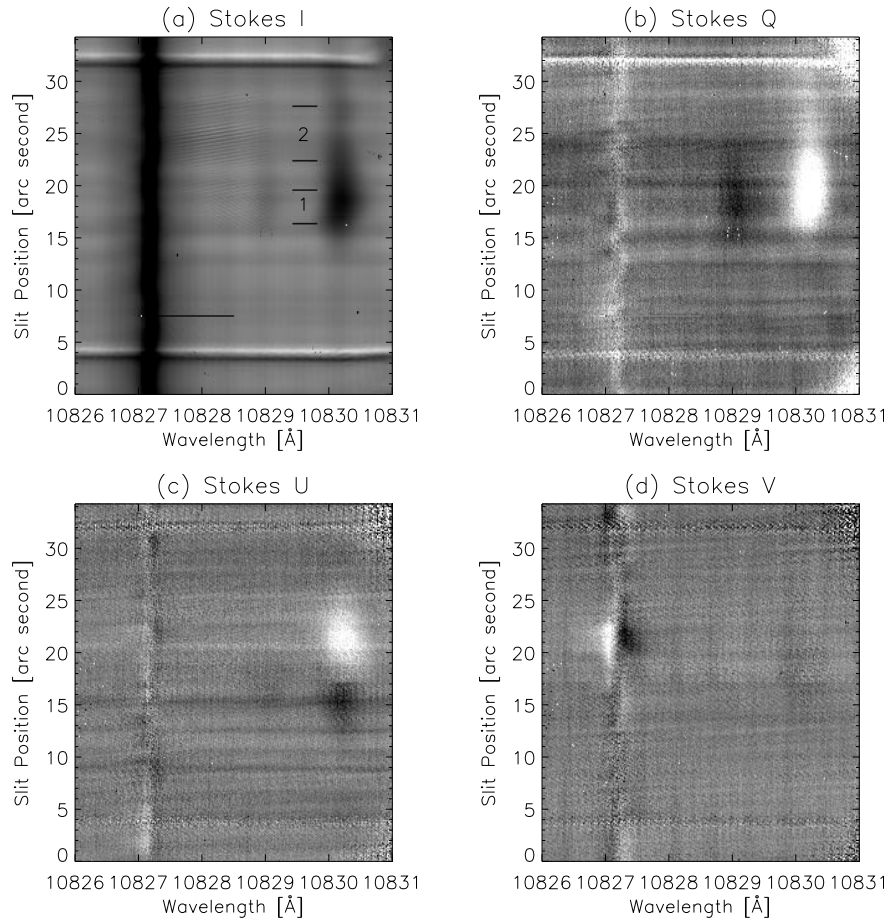


FIG. 2.—Stokes profiles of the filament at He I 10830 Å from the eighth scan step. The strong absorption line at 10827 Å is the neutral silicon line formed in the low photosphere. The central-depth ratio of the Stokes *I* profile at slit position 1 and 2 are used for the estimate of the optical density discussed in § 4.1.

are divided into two unipolar regions. Comparison between the Si I magnetogram and the He I Stokes *I* map indicated that the filament is located at the neutral line between the two unipolar regions. Figure 5 also shows that the Stokes *Q* polarization map closely resembles the Stokes *I* map. The Stokes *Q* is also the dominant polarization signal everywhere in the filament; it is due to the nonmagnetic resonance scattering polarization of radiation. The most interesting feature in the Stokes *U* map is the apparent polarization reversal on either side of the filament axis in section A in Figure 5. Since for our observations, the scattering geometry is different from the prominence observations, the Hanle effect diagnostic diagram for the He I 10830 Å line (Bommier 1978) cannot be used for the interpretation of our observations. We will derive a set of formulae for the non-90° magnetic scattering in the next section and interpret the polarization maps of Figure 5 in § 4.

3. POLARIZATION OF SCATTERED RADIATION IN THE PRESENCE OF A MAGNETIC FIELD

In this section, we will derive a set of diagnostic formulae for the filament polarization measurements, using classical electrodynamics only. We assume that the filament environment is optically thin and ignore the polarization from radiative transfer in a magnetized atmosphere (e.g., magneto-optical effects). We will first derive the formal solution for the scattering matrix of the Stokes vector, which is similar to the classical formulation of Stenflo

(1994). Next, we will derive a linearized solution using the weak-field approximation. The spirit of this exercise is to show more clearly the interaction between the polarization states of the scattered radiation and the magnetic field of the filament.

3.1. Scattering of Radiation

The classical electrodynamical theory of the scattering of radiation is described in Jackson (1975). To calculate the scattering radiation field, the equation of motion of a dipole located at the origin $\mathbf{r} = 0$ and excited by an external radiation field $\mathbf{E}_I e^{-i\omega t}$ is given by

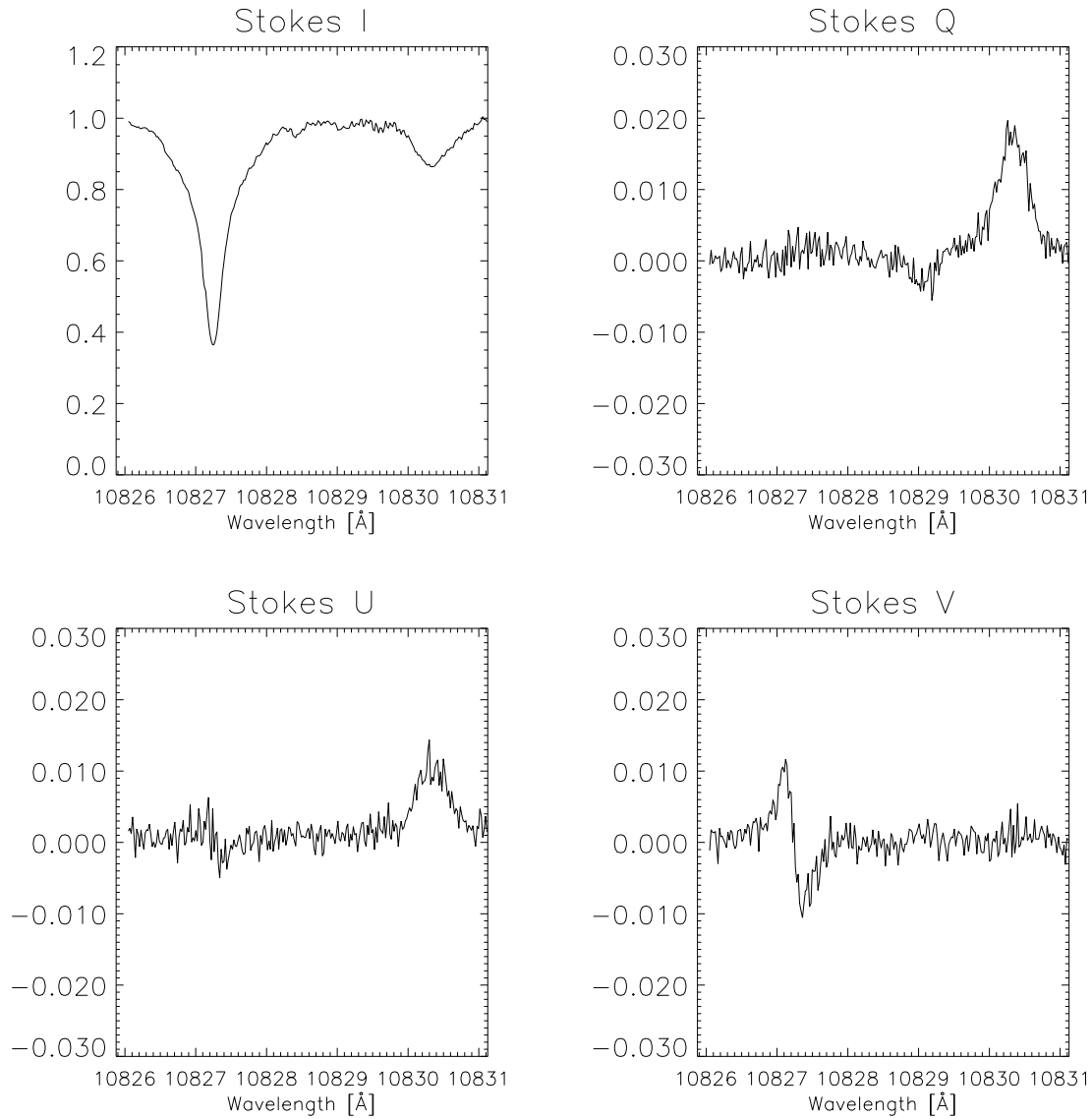
$$m \left(\ddot{\mathbf{x}} - \frac{e}{m} \dot{\mathbf{x}} \times \mathbf{B} + \Gamma \dot{\mathbf{x}} + \omega_0^2 \mathbf{x} \right) = e \mathbf{E}_I e^{-i\omega t}, \quad (1)$$

where Γ is the classical radiative dampening constant. The presence of the magnetic field \mathbf{B} defines a preferred orientation. In the circular polarization coordinate system defined by $(\hat{e}_+, \hat{e}_-, \hat{z})$, where $\hat{e}_\pm = [1/(2)^{1/2}](\hat{x} \pm i\hat{y})$ are the positive (+) and negative (−) unit circular polarization vectors, and \hat{z} is the unit vector in the direction of the magnetic field \mathbf{B} , equation (1) has simple solutions in the form of

$$x_q(\omega, t) = x_q(\omega) e^{-i\omega t}, \quad (2)$$

with

$$x_q(\omega) = \frac{e}{m} \frac{E_{Iq}}{\omega_0^2 - \omega^2 - 2q\omega\omega_B - i\Gamma\omega}, \quad (3)$$

FIG. 3.—Line plots of the Stokes profiles in Fig. 2, from slit position $y = 42''$

where $\omega_B = eB/2m$ is the Larmor frequency. The index $q = 0, 1$, and -1 corresponds to the \hat{z} , e_+ , and e_- polarization states. Finally, the scattered radiation field E_S at position r using the far-field approximation is given by

$$E_S(r, \omega, t) = -\omega^2 \frac{e^{-i(\omega t - \mathbf{k} \cdot \mathbf{r})}}{r} \hat{\mathbf{r}} \times \hat{\mathbf{r}} \times \mathbf{x}(\omega), \quad (4)$$

$$= \frac{e^{-i(\omega t - \mathbf{k} \cdot \mathbf{r})}}{r} E_S(\omega). \quad (5)$$

In order to derive expressions relevant to the observations, it is necessary to express the scattered radiation E_S of equation (4) in the observer's reference frame. On the other hand, the incident radiation E_I is most easily described in the local solar coordinate system of the filament since the incident radiation spans a solid angle symmetric around the local solar radial direction. Also, the scattering equation of the radiation field has normal modes in the coordinate system defined by the magnetic field

vector \mathbf{B} . Thus, there are three preferred coordinate systems that are relevant to our formulation: (1) the observer's reference frame $S_o \equiv (O; x, y, z)$, (2) the magnetic field coordinate system $S_m \equiv (O'; x', y', z')$, and (3) the scatterer's local coordinate system $S_s \equiv (O''; x'', y'', z'')$. The relative orientations between these three coordinate systems are shown in Figure 6. The orientation of S_o is such that z is in the line-of-sight direction, x is in the plane perpendicular to z and parallel to the solar limb, and y is in the plane perpendicular to z and parallel to the local radial direction. The magnetic field vector \mathbf{B} makes an angle γ with respect to z . The azimuthal angle between y' and y is denoted by χ . The angle between z'' and z is denoted by l . Finally, the direction of an incident photon with respect to the local solar coordinates system is characterized by the inclination angle θ and the azimuth angle ϕ .

With the coordinate systems defined as in Figure 6, we can calculate the scattered radiation field E_S given the incident radiation field E_I . Since the formulation is most easily described in matrix form, we will rewrite the oscillator solution of equation (3) in matrix form. Define the interaction

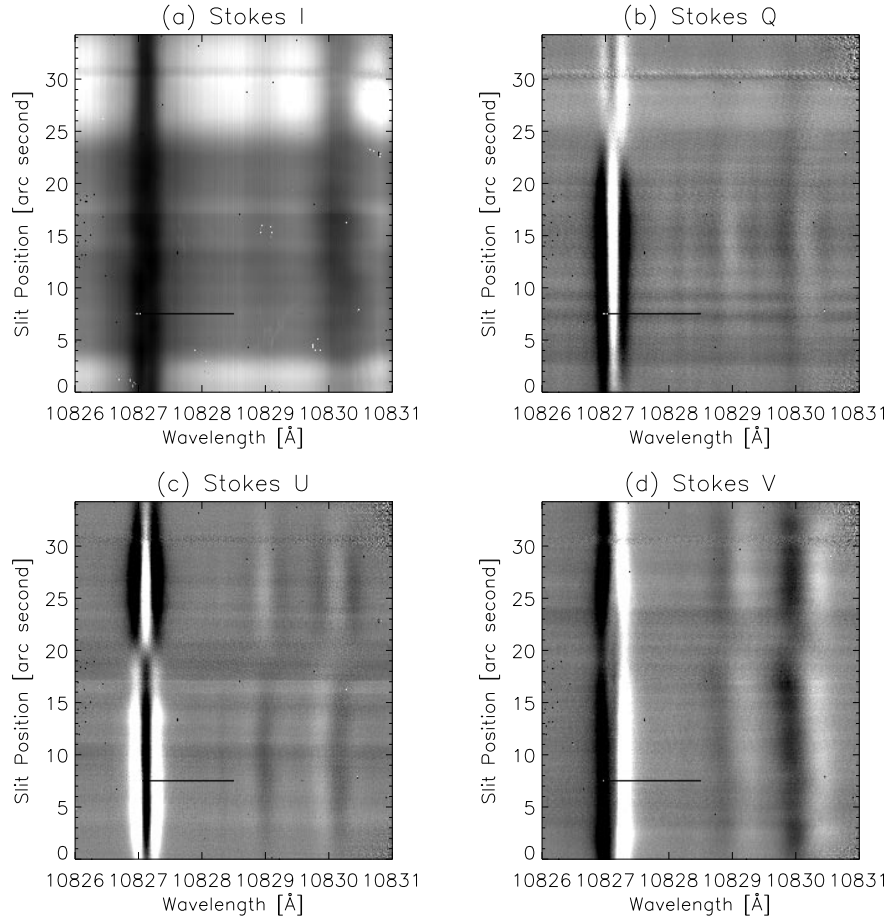


FIG. 4.—He I 10830 Å Stokes profiles across a sunspot umbra obtained right before the filament scan. The Si I 10827 Å line is used to calibrate the telescope and instrumental polarization cross talk. The small deviation from even symmetry of the Stokes Q and U profiles and the small π component in the Stokes V profile inside the umbra suggest that the telescope and instrumental polarization cross talk is small.

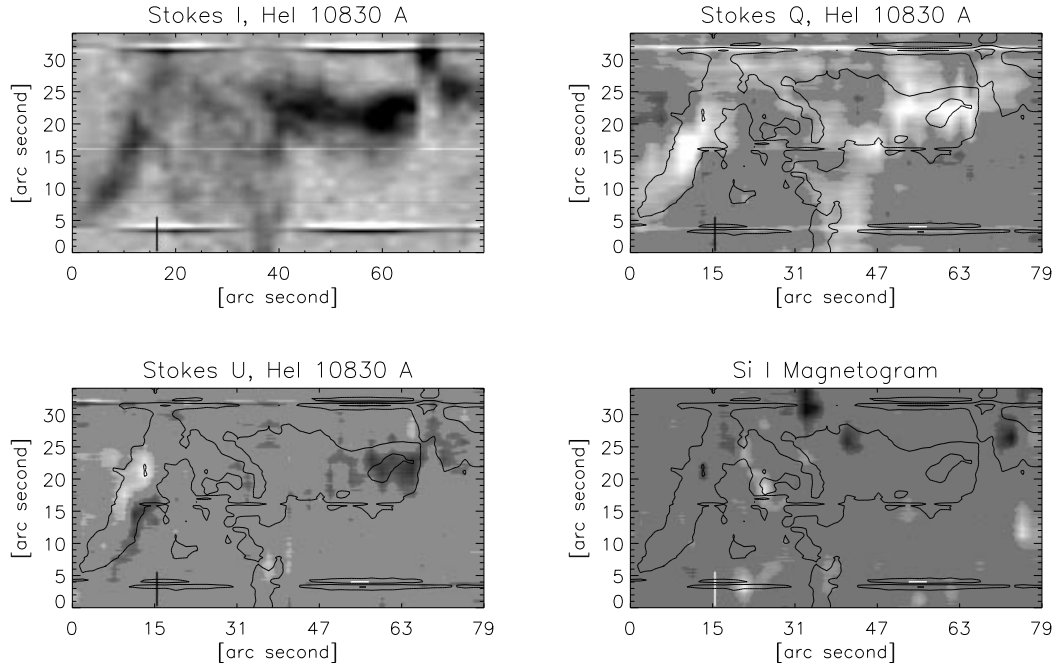


FIG. 5.—Integrated He I 10830 Å Stokes I , Q , and U intensity maps, and the photospheric magnetogram from the Stokes V profiles of the Si I 10827 Å line. The contours of the Stokes I intensity were overlaid in the Stokes Q , U intensity maps, and the Si I magnetogram. The dark vertical lines at position $x = 16''$ indicate the position where the Stokes spectra images in Fig. 2 was taken. A segment of the filament axis (at position $x = 70''$) was displaced when the correlation tracker lost track due to bad seeing.

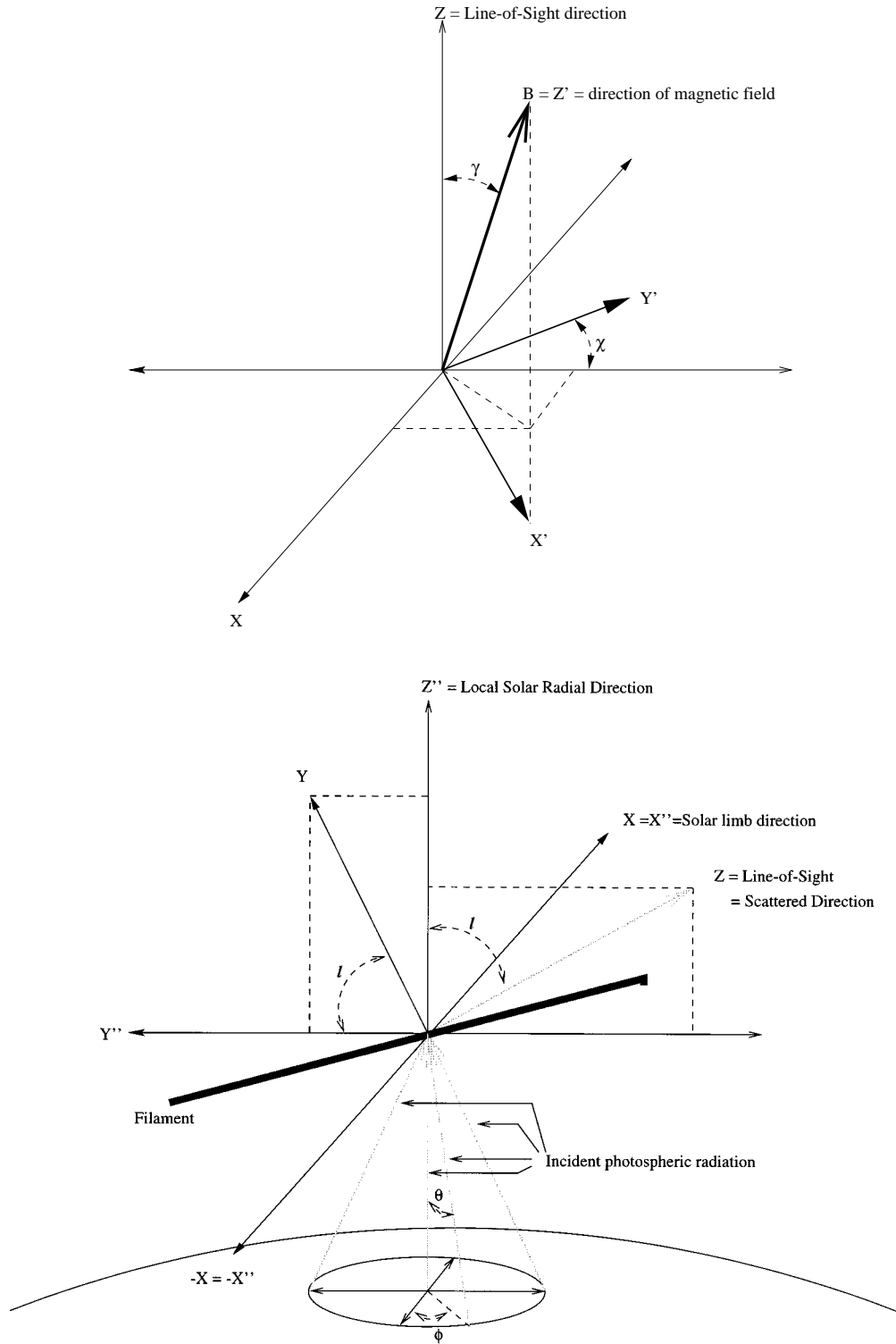


FIG. 6.—(Top) Relative orientation between the observer's coordinate system and the magnetic field. Inclination and azimuthal angles of the magnetic field vector with respect to the observer's coordinate system are γ and χ , respectively. (Bottom) Relative orientation between the local solar coordinates system, the observer's reference frame, and the filament axis. The filament is assumed to have one-dimensional structure, lying on the horizontal plane (the X'' - Y'' plane) parallel to the solar surface. The scattering angle of the principle incident radiation (along the Z'' axis) is l .

matrix N as

$$N \equiv \begin{bmatrix} N_+(\omega) & 0 & 0 \\ 0 & N_-(\omega) & 0 \\ 0 & 0 & N_0(\omega) \end{bmatrix}, \quad (6)$$

with

$$N_q(\omega) = \frac{e}{m} \frac{\omega^2}{\omega_0^2 - \omega^2 - 2q\omega\omega_B - i\omega\Gamma}. \quad (7)$$

The oscillator solution can be written as $X(\omega) = \omega - 2NE_I$.

Here X and E_I are the matrix representations of the oscillator solution and the incident radiation field, respectively.

To calculate the electric field of the scattered radiation, first we transform the incident electric field into the coordinate system of the magnetic field. This is achieved by a rotation matrix R which transforms the incident radiation coordinate system into the observer's coordinate system, followed by a rotation matrix P which transforms the observer's coordinate system into the magnetic field coordinate system. Next, we transform the incident radiation field into the circular polarization coordinate system using the transformation matrix ϵ between the circular polarization coordinate system and the Cartesian coordinate system. The equation of motion in equation (1) is then solved to obtain the oscillator solution by applying the interaction matrix N to the incident radiation field. The oscillator solution is then transformed back to the Cartesian coordinate system of magnetic field coordinate system by ϵ^{-1} , and then rotated back to the observer's reference frame using P^{-1} . Finally, we can obtain the electric field of the scattered radiation E_S in the observer's reference frame using the far-field approximation of equation (3). The explicit form of these coordinate transformation matrices can be found in the Appendix.

The above procedure can be expressed in matrix form as

$$E_S = \bar{r} P^{-1} \epsilon^{-1} N \epsilon P E_I, \quad (8)$$

$$= H R E_I, \quad (9)$$

$$= M E_I. \quad (10)$$

Here the phase factor $e^{-i(\omega t + \mathbf{k} \cdot \mathbf{r})/r}$ is left out of the equation, and equations (8)–(10) describe the scattering of only the time independent part of the electric field. In equation (8),

$$\bar{r} \equiv \begin{pmatrix} 1 & 0 & 0 \\ 0 & 1 & 0 \\ 0 & 0 & 0 \end{pmatrix},$$

since the term $-\hat{r} \times (\hat{r} \times \mathbf{x})$ simply extracts the x and y components of the vector \mathbf{x} . Equation (9) defines the forward scattering matrix $H \equiv \bar{r} P^{-1} \epsilon^{-1} N \epsilon P$ which describes the forward scattering problem. Its explicit form was derived in Jefferies, Lites, & Skumanich (1989). When combined with the coordinate transformation R , the scattering matrix $M \equiv H R$ in equation (10) describes the general scattering problem of an electric field.

3.2. Scattering of the Stokes Vector

The above formulation describes the scattering of a single photon off an atom in the presence of a magnetic field. Since the radiation field of a single photon is always 100% polarized, it cannot be used to describe the polarimetry data. To describe polarization observations, we need to formulate the scattering problem in the Stokes formulation. The Stokes formulation can be derived by way of the coherency matrix. The coherency matrix of a radiation field is

$$\begin{aligned} D &= (E E^\dagger)_{33} \equiv \begin{pmatrix} E_x & 0 \\ E_y & 0 \end{pmatrix} \begin{pmatrix} E_x^* & E_y^* \\ 0 & 0 \end{pmatrix} \\ &= \begin{pmatrix} E_x E_x^* & E_x E_y^* \\ E_y E_x^* & E_y E_y^* \end{pmatrix} \\ &= \begin{pmatrix} I + Q & U + iV \\ U - iV & I - Q \end{pmatrix}. \end{aligned} \quad (11)$$

We can write the coherency matrix of the scattered radiation as $D_S = M_{33} D_I M_{33}^\dagger$, where M_{33} is minor matrix formed by dropping the third row and third column of M . The Stokes vector I is related to the coherency matrix D by (Jefferies et al. 1989; Stenflo 1994)

$$I_k = \frac{1}{2} \text{Tr}(\sigma_k D), \quad (12)$$

where σ_k are the four Pauli spin matrices, and $I = (I, Q, U, V)$. From equations (10), (11), and (12) it is straightforward, although tedious, to derive the Stokes vector scattering equation:

$$\begin{pmatrix} I \\ Q \\ U \\ V \end{pmatrix}_S = \frac{1}{2r^2} \begin{pmatrix} m_{11} & m_{21} & m_{12} & m_{22} \\ m_{11} & -m_{21} & m_{12} & -m_{22} \\ m_{21} & m_{11} & m_{22} & m_{12} \\ im_{21} & -im_{11} & im_{22} & -im_{12} \end{pmatrix} \times \begin{pmatrix} m_{11}^* & m_{11}^* & m_{12}^* & im_{12}^* \\ m_{21}^* & m_{21}^* & m_{22}^* & im_{22}^* \\ m_{12} & -m_{12} & m_{11}^* & -im_{11}^* \\ m_{22}^* & -m_{22}^* & m_{21}^* & -im_{21}^* \end{pmatrix} \begin{pmatrix} I \\ Q \\ U \\ V \end{pmatrix}_I. \quad (13)$$

In equation (13), m_{ij} are the matrix elements from the i th row and the j th column of the general electric field scattering matrix M defined in equation (10). The scattering equation above can be decomposed into four terms, each describing the scattering of one of the four incident Stokes parameters. Since the net polarization of the solar photospheric radiation is small except near a large active region, $I_I = (I_I, 0, 0, 0)$, only the term involving the scattering of the incident Stokes I parameter is needed. Define a general scattering matrix $S_0(M, N)$ as

$$S_0(M, N) \equiv \frac{1}{2} \begin{pmatrix} m_{11} & m_{21} & m_{12} & m_{22} \\ m_{11} & -m_{21} & m_{12} & -m_{22} \\ m_{21} & m_{11} & m_{22} & m_{12} \\ im_{21} & -im_{11} & im_{22} & -im_{12} \end{pmatrix} \begin{pmatrix} n_{11}^* \\ n_{21}^* \\ n_{12}^* \\ n_{22}^* \end{pmatrix}. \quad (14)$$

Again, n_{ij} are the matrix elements from the i th row and the j th column of a matrix N . Using this definition of $S_0(M, N)$, the Stokes vector scattering equation (13) can be simplified to

$$I_S = \frac{1}{r^2} S_0(M, M) I_I. \quad (15)$$

The scattering matrix $S_0(M, N)$ was explicitly expressed as a function of two matrices M and N . In our case above, the second matrix is $N = M$. The reason for this definition of S_0 will become clear when we derive the Stokes vector scattering matrix using weak-field approximation.

I_S in equation (15) is the scattered Stokes vector per unit solid angle at a distance r away from the emitting dipole. From the perspective of the observer, the observed Stokes vector in a solid angle $d\Omega$ is $I d\Omega = I_S r^2 d\Omega$. Thus,

$$I = S_0(M, M) I_I \quad (16)$$

is the Stokes vector per unit solid angle received by the observer from the emitting atom.

3.3. Geometrical Depolarization Effects

Filaments are elevated structures above the solar photosphere illuminated by the photospheric radiation originating from an area which depends on the height of the filaments. The solid angle spanned by all of the incident radiation increases rapidly with decreasing height of the filaments. Since the limb darkening function at He I 10830 Å is a slow function of μ , the observed polarization signals consist of significant contributions from the nonradial incident radiation. In general, the effect of the nonradial incident radiation is to decrease the degree of polarization of the scattered radiation. This is the (nonmagnetic) geometrical depolarization.

Equations (13) and (16) describe the scattering of the Stokes vector from a single incident direction. To obtain the total scattered Stokes vector observed, we integrated the contributions from all incident directions:

$$\mathbf{I}(\mathbf{B}, l) = h^2 \int_{\theta=0}^{\theta_{\max}} \int_{\phi=0}^{2\pi} \mathbf{S}_0[\mathbf{M}(\mathbf{B}, l, \theta, \phi), \mathbf{M}(\mathbf{B}, l, \theta, \phi)] I_I(\theta, \phi) \sin \theta d\phi d\theta, \quad (17)$$

where θ_{\max} is the maximum incident angle with respect to the local solar radial direction. For a filament located at a height h (in units of solar radius) above the solar photosphere, $\theta_{\max} = \tan^{-1} [1/(2h)^{1/2}]$. Also, because the solar limb darkening function at He I 10830 Å is a slow function of μ , we will assume $I_I(\theta, \phi) = 1$. Consider an incident ray traveling toward the scattering atom with an inclination angle θ and an azimuth angle ϕ with respect to the local solar coordinate system. The geometrical transformation from the incident radiation frame to the observing frame is achieved first by a rotation of θ with respect to the y axis (in the coordinate system of the incident radiation) $\mathbf{R}_y(\theta)$, then a rotation of $-\phi$ with respect to the z axis (of the local solar coordinate system) $\mathbf{R}_z(-\phi)$, and finally a rotation of l with respect to the x axis $\mathbf{R}_x(l)$. The scattering equation of the electric field is

$$\begin{aligned} \mathbf{E}_S &= \mathbf{H}(\mathbf{B}) \mathbf{R}_x(l) \mathbf{R}_z(-\phi) \mathbf{R}_y(\theta) \mathbf{E}_I \\ &= \mathbf{M}(\mathbf{B}, l) \mathbf{R}_z(-\phi) \mathbf{R}_y(\theta) \mathbf{E}_I. \end{aligned} \quad (18)$$

By substitute $\mathbf{M}(\mathbf{B}, l, \theta, \phi) \equiv \mathbf{M}(\mathbf{B}, l) \mathbf{R}_z(-\phi) \mathbf{R}_y(\theta)$ into equation (17), and integrating over ϕ first, we obtain the Stokes vector scattering equation for all the incident radiation with incident angles between θ and $\theta + d\theta$:

$$\begin{aligned} \mathbf{I}(\mathbf{B}, l, \theta) &= \pi(1 + \cos^2 \theta) \mathbf{S}_0[\mathbf{M}(\mathbf{B}, l), \mathbf{M}(\mathbf{B}, l)] \\ &+ 2\pi(1 - \cos^2 \theta) \mathbf{S}_3[\mathbf{M}(\mathbf{B}, l), \mathbf{M}(\mathbf{B}, l)], \end{aligned} \quad (19)$$

where the function \mathbf{S}_3 is defined by

$$\mathbf{S}_3(\mathbf{M}, \mathbf{N}) \equiv \frac{1}{2} \begin{bmatrix} m_{13} n_{13}^* + m_{23} n_{23}^* \\ m_{13} n_{13}^* - m_{23} n_{23}^* \\ m_{13} n_{23}^* + m_{23} n_{13}^* \\ -i(m_{13} n_{23}^* - m_{23} n_{13}^*) \end{bmatrix}, \quad (20)$$

and m_{ij} is the matrix element from the i th row and j th column of the scattering matrix $\mathbf{M}(\mathbf{B}, l)$. \mathbf{S}_3 involves only the third column of \mathbf{M} and \mathbf{N} . Integrating over θ , we obtain the integrated Stokes vector scattering equation:

$$\mathbf{I}(\mathbf{B}, l) = (C_1 + C_2) \mathbf{S}_0 + 2(C_1 - C_2) \mathbf{S}_3, \quad (21)$$

$$C_1 = \pi h^2 (1 - \cos \theta_{\max}), \quad (22)$$

$$C_2 = \frac{\pi h^2}{3} (1 - \cos^3 \theta_{\max}). \quad (23)$$

Since $\mathbf{M}(\mathbf{B}, l)$ is the electric field scattering matrix of the principal incident radiation traveling along the radial direction, \mathbf{S}_0 is just the Stokes vector scattering matrix of the principal incident radiation which depends only on the first and second column of the scattering matrix $\mathbf{M}(\mathbf{B}, l)$, and \mathbf{S}_3 is the geometrical depolarizing term that depends only on the third column of $\mathbf{M}(\mathbf{B}, l)$. In this formulation, we only need to consider the scattering matrix of the principal (radial) incident radiation. This greatly reduces the complexity of the scattering matrix of the Stokes vector.

3.4. Weak-Field Approximation

The Stokes scattering matrix in equations (13) and (20) depends on the sums of the square of the elements of the electric field scattering matrix \mathbf{M} . It is difficult to visualize how each Stokes parameter depends on the magnetic field. Prominence observations (Leroy 1989) showed that the magnetic field strength in the filaments are of the order of a few tens of Gauss. Thus, ω_B is small compared with the Doppler width of the He I 10830 Å line. Therefore, it is possible to formulate the scattering problem with the weak-field approximation. This weak-field approximation will show more clearly the relationship between the observed Stokes profiles and the filament magnetic field.

When ω_B is small, we can expand the elements of the interaction matrix $N(\omega)$ in Taylor series in terms of ω_B :

$$\begin{aligned} N_q(\omega) &= N_0(\omega + q\omega_B) \\ &\approx N_0(\omega) + qN'_0(\omega)\omega_B + \frac{1}{2}q^2N''_0(\omega)\omega_B^2 + \cdots, \end{aligned} \quad (24)$$

where $N'_0(\omega)$ and $N''_0(\omega)$ are the first- and second-order derivatives of $N_0(\omega)$, respectively; and $q = 0, \pm 1$ are the three polarization states in the circular polarization representation. For the simplicity of the notation we will use $N(\omega) \equiv N_0(\omega)$. The interaction matrix \mathbf{N} can now be written as

$$\begin{aligned} \mathbf{N} \equiv N(\omega) &\begin{pmatrix} 1 & 0 & 0 \\ 0 & 1 & 0 \\ 0 & 0 & 1 \end{pmatrix} + N'(\omega)\omega_B \begin{pmatrix} 1 & 0 & 0 \\ 0 & -1 & 0 \\ 0 & 0 & 0 \end{pmatrix} \\ &+ \frac{1}{2}N''(\omega)\omega_B^2 \begin{pmatrix} 1 & 0 & 0 \\ 0 & 1 & 0 \\ 0 & 0 & 0 \end{pmatrix} + \cdots. \end{aligned} \quad (25)$$

Using equation (25) in equation (10), we can express the electric field scattering matrix $\mathbf{M}(\mathbf{B}, l)$ of the principal incident radiation by a power series expansion of ω_B :

$$\begin{aligned} \mathbf{M}(\mathbf{B}, l) &= N(\omega)\mathbf{M}^{(0)}(\mathbf{B}, l) + N'(\omega)\mathbf{M}^{(1)}(\mathbf{B}, l)\omega_B \\ &+ \frac{1}{2}N''(\omega)\mathbf{M}^{(2)}(\mathbf{B}, l)\omega_B^2. \end{aligned} \quad (26)$$

In this expression, $N(\omega)\mathbf{M}^{(0)}$ is the nonmagnetic scattering term, and $N'(\omega)\mathbf{M}^{(1)}$ and $N''(\omega)\mathbf{M}^{(2)}$ are the first- and second-order magnetic scattering terms. The explicit forms of $\mathbf{M}^{(i)}$ can be found in the Appendix.

From equation (26), and assuming an unpolarized incident radiation $\mathbf{I}_I = (1, 0, 0, 0)$, it follows immediately that the Stokes vector scattering matrix of the principal incident

radiation is

$$S_0 = S_0^{(0)} + S_0^{(1)}\omega_B + \frac{1}{2}S_0^{(2)}\omega_B^2, \quad (27)$$

with

$$S_0^{(0)} = N(\omega)N^*(\omega)S_0[M^{(0)}, M^{(0)}], \quad (28)$$

$$S_0^{(1)} = N(\omega)N'^*(\omega)S_0[M^{(0)}, M^{(1)}] \\ + N'(\omega)N^*(\omega)S_0[M^{(1)}, M^{(0)}], \quad (29)$$

$$S_0^{(2)} = N(\omega)N''^*(\omega)S_0[M^{(0)}, M^{(2)}] \\ + N''(\omega)N^*(\omega)S_0[M^{(2)}, M^{(0)}] \\ + 2N'(\omega)N'^*(\omega)S_0[M^{(1)}, M^{(1)}]. \quad (30)$$

Following the same derivation for equation (21), the geometrical depolarizing Stokes scattering matrix S_3 can be expressed as a power series of ω_B as in equation (27), replacing the subscript 0 with a subscript 3. The definition of the zeroth-, first-, and second-order terms of S_3 are identical to equations (28)–(30), replacing the subscript 0 by subscript 3. The observed Stokes vector including the geometrical depolarizing effect is identical to equation (21), replacing S_0 and S_3 with their corresponding power series expansion representations.

For a filament observation on the disk at position $\mu = \cos l$, the coordinate transformation from the principal incident radiation frame to the observing frame is:

$$R = \begin{pmatrix} 1 & 0 & 0 \\ 0 & \cos l & \sin l \\ 0 & -\sin l & \cos l \end{pmatrix}. \quad (31)$$

It is then straightforward to derive the normal and geometrical depolarizing Stokes vector I_0 , and I_3 :

$$I_0 = \frac{1}{2}NN^*(1 + \cos^2 l) - \text{Re}(iNN'^*)\omega_{Bx} \sin l \cos l, \quad (32a)$$

$$Q_0 = \frac{1}{2}NN^*(1 - \cos^2 l) + \text{Re}(iNN'^*)\omega_{Bx} \sin l \cos l, \quad (32b)$$

$$U_0 = -\text{Re}(iNN'^*)[\omega_{Bz}(1 - \cos^2 l) - \omega_{By} \sin l \cos l], \quad (32c)$$

$$V_0 = -\text{Im}(iNN'^*)[\omega_{Bz}(1 + \cos^2 l) + \omega_{By} \sin l \cos l], \quad (32d)$$

$$I_3 = \frac{1}{2}NN^* \sin^2 l + \text{Re}(iNN'^*)\omega_{Bx} \sin l \cos l, \quad (32e)$$

$$Q_3 = -\frac{1}{2}NN^* \sin^2 l - \text{Re}(iNN'^*)\omega_{Bx} \sin l \cos l, \quad (32f)$$

$$U_3 = \text{Re}(iNN'^*)(\omega_{Bz} \sin^2 l - \omega_{By} \sin l \cos l), \quad (32g)$$

$$V_3 = -\text{Im}(iNN'^*)(\omega_{Bz} \sin^2 l - \omega_{By} \sin l \cos l), \quad (32h)$$

where $\omega_{Bx} = \omega_B \sin \gamma \cos \chi$ is the horizontal part of the transverse component, and $\omega_{By} = \omega_B \sin \gamma \sin \chi$ is the transverse component parallel to the local solar radial vector, and $\omega_{Bz} = \omega_B \cos \gamma$ is the longitudinal component of ω_B along the line-of-sight direction, respectively. We only derived the Stokes vector to the first order in ω_B . This is sufficient for the filament observation with $l \neq 90^\circ$. The

second order terms can be found in the Appendix, which will be used in the discussion of the prominence Hanle effect.

So far, we only considered the scattering problem in the rest frame of the scattering atoms, and the frequency-dependent parts of the Stokes vector, NN^* , $\text{Re}(iNN'^*)$, and $\text{Im}(iNN'^*)$, only include the radiative damping broadening effects. Although the He I 10830 Å line is composed of three wavelength components, we will treat only the main blended component and consider it as a single spectral line. The derivation to include the Doppler broadening effects has been treated in many places (e.g., Mihalas 1978). Using the approximation that $(\omega/\omega_0) \approx 1$ and

$$N(\omega) \approx \frac{e\omega_0}{2m} \frac{1}{(\omega_0 - \omega) - i\Gamma/2}, \quad (33)$$

the frequency dependent functions of the Stokes vector are

$$N^* = \left(\frac{e\omega_0}{2m}\right)^2 \frac{1}{(\omega_0 - \omega)^2 + (\Gamma/2)^2}, \quad (34)$$

$$\text{Re}(iNN'^*) = \left(\frac{e\omega_0}{2m}\right)^2 \frac{\Gamma/2}{[(\omega_0 - \omega)^2 + (\Gamma/2)^2]^2}, \quad (35)$$

$$\text{Im}(iNN'^*) = \left(\frac{e\omega_0}{2m}\right)^2 \frac{(\omega_0 - \omega)}{[(\omega_0 - \omega)^2 + (\Gamma/2)^2]^2}. \quad (36)$$

Following Mihalas (1978), the Doppler-broadened profiles can be obtained by convolving the damping profiles in equations (34)–(36) with a Maxwellian velocity distribution function

$$W(\xi)d\xi = (\pi^{1/2}\xi_0)^{-1}e^{(-\xi^2/\xi_0^2)}d\xi, \quad (37)$$

where ξ is the velocity of the atom in the observer's rest frame, and $\xi_0 = (2kT/m)^{1/2}$ is the thermal velocity of the atmosphere. The resulting Stokes profiles are

$$I_0 = h(a, v)(1 + \cos^2 l) - k(a, v)\omega_{Bx} \sin l \cos l, \quad (38a)$$

$$Q_0 = h(a, v)(1 - \cos^2 l) + k(a, v)\omega_{Bx} \sin l \cos l, \quad (38b)$$

$$U_0 = k(a, v)[\omega_{By} \sin l \cos l - \omega_{Bz}(1 - \cos^2 l)], \quad (38c)$$

$$V_0 = -f(a, v)[\omega_{By} \sin l \cos l + \omega_{Bz}(1 + \cos^2 l)], \quad (38d)$$

$$I_3 = h(a, v) \sin^2 l + k(a, v)\omega_{Bx} \sin l \cos l, \quad (38e)$$

$$Q_3 = -h(a, v) \sin^2 l - k(a, v)\omega_{Bx} \sin l \cos l, \quad (38f)$$

$$U_3 = k(a, v)(\omega_{Bz} \sin^2 l - \omega_{By} \sin l \cos l), \quad (38g)$$

$$V_3 = -f(a, v)(\omega_{Bz} \sin^2 l - \omega_{By} \sin l \cos l), \quad (38h)$$

where

$$h(a, v) \equiv \frac{1}{2} \int_{-\infty}^{\infty} NN^* \left(\omega - \omega \frac{\xi}{c} \right) W(\xi) d\xi \\ = \frac{\sqrt{\pi} e^2 \omega_0^2 a}{8m^2 \Delta \omega_D^2 \pi} \int_{-\infty}^{+\infty} \frac{e^{-y^2} dy}{(v - y)^2 + a^2} \\ = \frac{\sqrt{\pi} a e^2 \omega_0^2}{8m^2 \Delta \omega_D^2} H(a, v), \quad (39)$$

$$k(a, v) \equiv \int_{-\infty}^{\infty} \text{Re} \left[iNN'^* \left(\omega - \omega \frac{\xi}{c} \right) \right] W(\xi) d\xi \\ = \frac{e^2 \omega_0^2}{4\sqrt{\pi} m^2 \Delta \omega_D^3} \int_{-\infty}^{+\infty} \frac{a e^{-y^2} dy}{[(v - y)^2 + a^2]^2}, \quad (40)$$

$$f(a, v) \equiv \int_{-\infty}^{\infty} \text{Im} \left[iNN^* \left(\omega - \omega \frac{\xi}{c} \right) \right] W(\xi) d\xi \\ = \frac{e^2 \omega_0^2}{4\sqrt{\pi} m^2 \Delta \omega_D^3} \frac{1}{\pi} \int_{-\infty}^{+\infty} \frac{(v-y)e^{-y^2} dy}{[(v-y)^2 + a^2]^2}, \quad (41)$$

$$v \equiv (\omega - \omega_0)/\Delta \omega_D, \quad (42)$$

$$y \equiv (\Delta \omega/\Delta \omega_D), \quad (43)$$

$$a \equiv \Gamma/2 \Delta \omega_D, \quad (44)$$

where $\Delta \omega_D \equiv \xi_0 \omega_0/c$ is the Doppler width of the line, and $H(a, v)$ is the Voigt function. In equation (38), the Stokes I , Q , and U states only depend on $h(a, v)$ and $k(a, v)$, which are symmetric around the line center ω_0 . Thus the Stokes Q and U line profiles are similar to the Stokes I profile. The frequency-dependent function of the Stokes V profile $f(a, v)$ is antisymmetric around ω_0 . Since the damping width is much narrower than the Doppler width, the Doppler-broadening reduces the net Stokes V amplitude. This explains that the Hanle effect Stokes V signals are typically 1 order of magnitude smaller than the linear polarization signals.

3.5. Prominence Hanle Effects: 90° Scattering

The validity of the weak-field approximation can be verified against the well-known Hanle effect of prominences. The qualitative properties of prominence Hanle effects are (1) depolarization due to the presence of a transverse magnetic field in the horizontal direction, (2) depolarization and rotation of the linear polarization plane due to a longitudinal magnetic field, (3) the insensitivity to the vertical component of the magnetic field, and (4) 180° ambiguity of the direction of the transverse magnetic field. Since the Stokes V signal is typically small, we will ignore its effect. For simplicity, we will also use only the normal scattered Stokes vector for the discussion here, ignoring the geometrical depolarization effects.

When observing at the limb, $l = 90^\circ$, equations (38a)–(38h) (including second-order terms from the Appendix) reduce to

$$I_0 = h(a, v) + \frac{1}{\Gamma} k(a, v) \omega_B^2, \quad (45a)$$

$$Q_0 = h(a, v) - \frac{1}{\Gamma} k(a, v) \omega_B^2 \\ \times [\cos^2 \gamma + \sin^2 \gamma (\cos^2 \chi - \sin^2 \chi)], \quad (45b)$$

$$U_0 = -k(a, v) \omega_B \cos \gamma. \quad (45c)$$

When there is only a transverse field, $\gamma = 90^\circ$, equation (45) reduces to

$$I_0 = h(a, v) + \frac{1}{\Gamma} k(a, v) \omega_B^2, \quad (46a)$$

$$Q_0 = h(a, v) - \frac{1}{\Gamma} k(a, v) \omega_B^2 \cos 2\chi, \quad (46b)$$

$$U_0 = 0. \quad (46c)$$

This describes the Hanle depolarization due to a transverse magnetic field. Note that the magnetic term in the Stokes Q

profile in equation (46b) depends on the square of ω_B . It is clear that the Stokes Q profile is insensitive to inversion of the direction of the magnetic field. Thus, the 180° ambiguity in the direction of the magnetic field is also contained in equations (46a)–(46c). When the magnetic field is in the vertical direction, $\chi = 90^\circ$, then $I_0 = Q_0 = h(a, v) + (1/\Gamma)k(a, v)\omega_B^2$. There is no depolarization. Thus, the Hanle effect of prominence observation is not sensitive to the vertical component of the magnetic field. Finally, when there is only longitudinal field, $\gamma = 0^\circ$, and equations (45a)–(45c) reduce to

$$I_0 = h(a, v) + \frac{1}{\Gamma} k(a, v) \omega_B^2, \quad (47a)$$

$$Q_0 = h(a, v) - \frac{1}{\Gamma} k(a, v) \omega_B^2, \quad (47b)$$

$$U_0 = -k(a, v) \omega_B. \quad (47c)$$

Thus, the longitudinal field generates a nonzero Stokes U state, as well as the depolarization of the Stokes Q state. This is the Hanle depolarization and rotation of the polarization plane due to the presence of a longitudinal magnetic field.

4. FILAMENT MAGNETIC FIELD CONFIGURATION

Filaments consist of cool gas floating in the hot solar corona against gravity. To date, most of the filament magnetic field models are based on two key observations, namely, (1) the observation of the photospheric magnetic field distribution around filaments of Babcock & Babcock (1955), and (2) the prominence Hanle effect observations. Following the discovery that filaments are located at the neutral line between two large unipolar magnetic regions on the solar photosphere (Babcock & Babcock 1955), Kippenhahn & Schlüter (1957, KS model) first suggested that the filament material sits in the dip at the top of the magnetic field lines that connect the two unipolar regions. Kuperus & Raadu (1974, KR model) later proposed that a closed-loop magnetic field can also support the filament materials as well as shield them from the hot coronal plasma. Since the filament magnetic field in the KS model points in the same direction as the direction of the magnetic field connecting the unipolar regions on the opposite side of the filament, it is usually referred to as the normal configuration. The KR model, on the other hand, was referred to as the inverse configuration because the filament magnetic field points in the opposite direction of the surrounding large-scale field. Both models are two-dimensional with the magnetic field confined in a vertical plane with respect to the solar surface. Although both are viable models, there were no observational tests that can distinguish them until the utilization of the prominence Hanle effect. With the advances of the prominence Hanle effect observations, Leroy et al. (1984), for the first time, was able to distinguish the sense of the magnetic field across the filament (normal vs. inverse). Later Leroy (1989) also showed that filaments actually possess a strong magnetic field along the axial direction. These new results led to the development of many three-dimensional magnetic field models. These models can be classified into three categories: (1) a KS model with an axial component, (2) a KR model with an axial component, and (3) the empirical model proposed by Martin & Echols (1994). A helical magnetic field configuration can be con-

sidered as the KR model with an axial field. Unfortunately the prominence Hanle effect cannot be used to distinguish between these new models, but this new He I 10830 Å filament polarimetry can provide constraining observations. In this section, we will first discuss the diagnostics capability of the He I 10830 Å polarimetry of the filament, and then we will apply it to our data to derive a magnetic field configuration for the filament we observed.

4.1. Filament Magnetic Field Diagnostics

When discussing the magnetic field configuration of a filament, it is sometimes more intuitive to use the local solar coordinate system. Applying the coordinate transformation between the observer's coordinate system and the local solar coordinate system, the normal and the geometrical depolarizing term of the Stokes vector can be rewritten as

$$I_0 = h(a, v)(1 + \cos^2 l) - k(a, v)\omega_{B_x''} \sin l \cos l, \quad (48a)$$

$$Q_0 = h(a, v)(1 - \cos^2 l) + k(a, v)\omega_{B_x''} \sin l \cos l, \quad (48b)$$

$$U_0 = k(a, v)\omega_{B_y''} \sin l, \quad (48c)$$

$$V_0 = f(a, v)(\omega_{B_y''} \sin l - 2\omega_{B_z''} \cos l), \quad (48d)$$

$$I_3 = h(a, v) \sin^2 l + k(a, v)\omega_{B_x''} \sin l \cos l, \quad (48e)$$

$$Q_3 = -h(a, v) \sin^2 l - k(a, v)\omega_{B_x''} \sin l \cos l, \quad (48f)$$

$$U_3 = -k(a, v)\omega_{B_y''} \sin l, \quad (48g)$$

$$V_3 = f(a, v)\omega_{B_y''} \sin l, \quad (48h)$$

According to equations (48a)–(48h), the linear polarizations (the Stokes Q and U) are only sensitive to the horizontal magnetic field parallel to the local solar surface. The more interesting feature is that when $l \neq 90^\circ$, the circular polarization of the scattered radiation is sensitive to the vertical component of the magnetic field B_z'' . Therefore, the complete vector magnetic field configuration of a filament can be determined from the full Stokes profile measurement provided that we also measure the height of the filament. This is a major advantage compared with limb observations of prominences in which usually two complementary observations are required to determine the full vector magnetic field (Bommier, Leroy, & Sahal-Br  chot 1981). The disadvantage, of course, is that the height of the filament is more difficult to measure. We assume that the filament rises vertically into the solar corona and that the footpoint of the filament is anchored at the photosphere. Knowing its position on the solar disk, the height can be inferred from the projected vertical distance between the footpoint and the top of the filament. Using this method, the estimated height of the filament is of the order of 34,000 km. The maximum polarization according to equation (20) is approximately 3%. This is consistent with the observed polarization of the filament.

The vertical field sensitivity of the Stokes V signal in equation (48d) is valid only when the circular polarization signals are due purely to single scattering processes, that is, if the scattering atmosphere is optically thin. In the chromospheric level, de Jager, Namba, & Neven's (1966) measurement showed that the He I 10830 Å line is actually formed in fairly optically thick regions. They derived an average optical density of 2 for the chromospheric major component of the He I 10830 Å line radiation. To estimate the optical thickness of the filament, we measured the ratio of

the central line depths r between the blended major component of the He I 10830 Å triplet (wavelength 10830.3 Å) and the blue component at 10829.1 Å from two sections of the filament labeled 1 and 2 in the Stokes I spectrum shown in Figure 2. Figure 7 shows the average profiles from filament sections 1 and 2. The measured central-depth ratios for slit position 1 and 2 are $r_1 = 4.4$ and $r_2 = 8.1$, respectively. The Doppler widths at the two positions are both $\Delta\lambda_D = 0.23$ Å. Using the theoretical curve of the central-depth ratio as a function of the optical thickness, (eq. [5] and Fig. 7 in de Jager et al. 1966), we derived an optical thickness of $\tau_0(10830) \approx 2$ for filament section 1, and $\tau_0(10830) \approx 0$ for filament section 2.

In an optically thick atmosphere with low electron density like filament section 1 in Figure 2, the incident photospheric photons may experience many scattering events before they emerge from the scattering atmosphere. Under such circumstances, radiative transfer formulation may be required for proper interpretation of the observational data. This is beyond the scope of the present paper, and we will defer it to future work. At section 2, there were significant Stokes Q polarizations in the major component in the He I 10830 Å triplet. However, both the Stokes Q polarization in the blue 10829.1 Å component and the Stokes U polarization are weak. The central-depth ratio r at this position is 8, approaching the theoretical ratio for an optically thin atmosphere. The circular polarization signals from this region should be well described by equation (48).

Given sufficient signal-to-noise ratio, the filament polarization measurement offers interesting diagnostics that should allow us to test the competing filament magnetic field models. For example, one can use the Stokes V observation to test the assumption that the cool filament materials are supported by a dip in the magnetic field lines at the top of the loop, such as the KS and KR model. If this is indeed the material support structure, the vertical fields

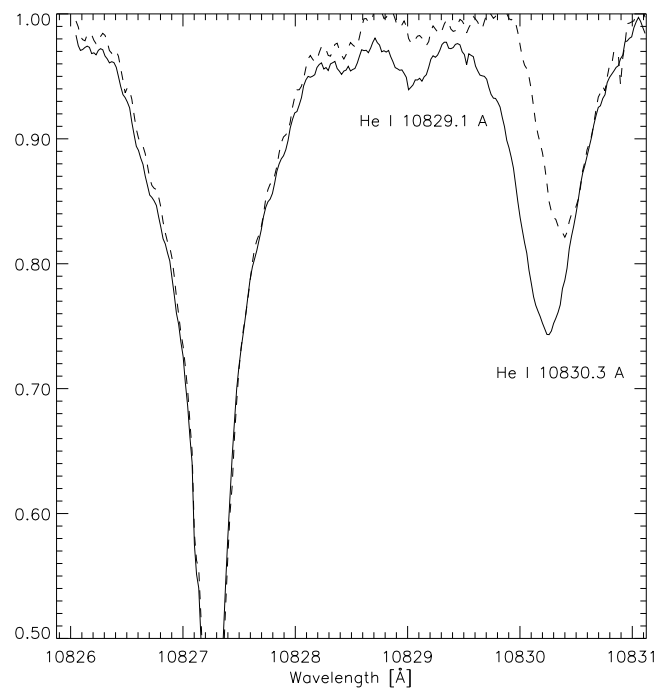


FIG. 7.—Stokes I profiles from filament section 1 (solid line) and 2 (dash line) shown in Fig. 2.

on either side of the filament axis should point in opposite directions. In comparison, the empirical model proposed by Martin & Echols does not have a dip in the magnetic field line as the support mechanism. The relative orientation of the dip with respect to the direction of the large-scale loop between the unipolar regions should allow us to determine if the horizontal transaxial field is in a normal or inverse configuration. Of course, direct measurements of the horizontal transaxial field have the same diagnostics capability. One can also test the helical field configuration by observing the transaxial field reversal on either side of the filament axis at different disk positions: a helical field configuration should show transaxial field reversal on either side of the axis regardless of disk position, while a non-helical field configuration should not.

4.2. Interpretation of the Data

In our first filament polarization observation, we did not have enough sensitivity to measure the Stokes V polarization. Thus we do not have information about the vertical component of the magnetic field. Also, because we do not have a reliable estimate of the height of the filament, we will not attempt to decouple the magnetic effect from the non-magnetic scattering polarization in the Stokes Q signals. Therefore, we will only discuss the implication of the Stokes U polarization concerning the filament magnetic field since the Stokes U polarization is purely magnetic in origin. Incidentally, the Stokes U map in Figure 5 is also the most interesting result of this observation. It shows that in the first section (A) of the observed filament, the Stokes U states reverse polarity from one side of the filament axis to the other. In section B, the filament axis changes its apparent orientation, bending toward the west. The Stokes U polarization in this part of the filament does not change sign.

The axis of section A of the filament is roughly aligned with the radial direction of the solar disk. Thus, the axial field lies in the y'' direction, and the horizontal transaxial field lies in the x'' direction. Since the Stokes U polarization is purely magnetic, and is only sensitive to $\omega_{By''}$, the Stokes U reversal implies that the axial fields on either side of the filament are pointing in opposite directions. Interestingly, this feature is not predicted by any of the existing filament magnetic field models. The magnetic field arcades in both the KS and KR model are confined in a vertical plane with respect to the solar surface and do not contribute to a field component in the direction of the filament axis. Leroy (1989) first showed the existence of the axial field, however, his observation did not show any sign of axial field reversal. Subsequently, all the three-dimensional magnetic field models incorporated an axial field with a single direction.

One possible magnetic field configuration that can generate the observed axial field reversal on either side of the filament axis is a tilted magnetic field loop (Fig. 8). Consider a KR-type arcade being pushed at the top along the direction of the axis of the filament with the footpoints fixed. If such a tilted loop does exist, then the axial component on either side of the loop must point in opposite directions. Similarly, a tilted KS type field configuration will show the same axial field reversal. Although this configuration has not been specifically described in existing models, there is no theoretical reason to rule it out. In fact, tilted loops are a common feature in force-free numerical simulations of three-dimensional magnetic field structure over active regions (Sakurai 1989; Chou & Low 1994). Obser-

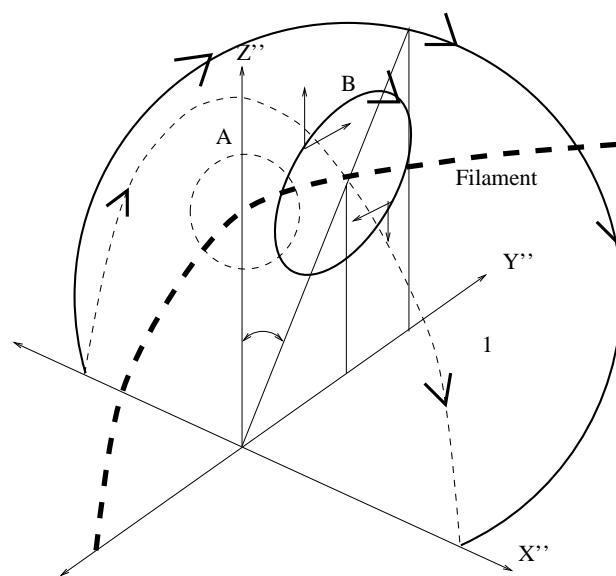


FIG. 8.—Model of a tilted KR type magnetic field configuration that can generate the observed axial field reversal on either side of the filament axis. The vertical loop A (dashed complete circle) does not have an axial component. The tilted loop B (solid complete circle) possesses opposite axial fields on either side of the filament.

vationally, we can use X-ray images, such as those from the *Yohkoh* satellite, to search for evidence of tilted magnetic field loops. However it may be difficult to determine the exact tilt angle of the loops due to the projection effect. Inspection of these X-ray images also gives a strong impression that tilted loops exist in abundance. Therefore, the tilted magnetic field loop is a possible explanation for the observed axial field reversal.

In section B of the filament, the filament axis turned about 20° toward the west. Thus, we are only observing one side of the filament. The Stokes U polarization on the two sides of the filament axis did not reverse polarity in this part of the filament. Since we only see one side of the filament, we do not expect to see the axial field reversal. This is consistent with the tilted magnetic field loop model we proposed above. This observing angle selection effect is also possibly the reason that the prominence Hanle effect observations have not measured the axial field reversal: we can only see both sides of a prominence if we observe it edge-on, which is a rare occasion. Most of the previous prominence magnetic field measurements in the literature observed prominence from the side. Therefore, the axial field reversal would have easily escaped detection.

5. SUMMARY AND FUTURE PROSPECTS

We presented the first Stokes polarization measurement of a filament using the He I 10830 Å line. Using a simple classical formulation, we derived a set of diagnostic formulae that can be used to determine the magnetic field configuration of filaments. We showed evidence that the magnetic field along the axis of the filament reverses direction on either side of the axis. We also proposed a tilted magnetic field loop as the possible magnetic field configuration of the observed axial field reversal.

This experiment reveals some of the magnetic field structure that has been difficult to detect from limb observations. At this early stage, it serves to demonstrate the potential of

He I 10830 Å polarimetry as a tool for the study of filament magnetic fields. The classical model used in this work provides an excellent starting point for developing simple expressions for the Stokes vectors. However, the classical model has many deficiencies. For example, it fails to explain the reversal of the Stokes Q vector between the main He component (10830.3 Å) and the blue He component (10829.1 Å) observed in some regions of the filament (see Fig. 2); an examination of the physics of all the He I 10830 Å spectral components may resolve this issue. This work also provides direction for future development of instrumentation and observational techniques. For example, one can imagine that continuous magnetic field measurements of an active filament erupting event can yield invaluable information on the physics of coronal mass ejections. Similar time series can also be used for the study of the evolution of filaments and the dynamics of coronal magnetic fields. Also, it is clear that we need to further reduce the noise in the polarization spectra substantially in order to accurately

measure the Stokes V profile. These observational requirements are certain to provide inspiration for the next generation of high-speed, high-precision infrared instrumentation.

The author (H. L.) is grateful to Jack Zirker and Sara Martin for many discussions on the subject of filament observations and theory, as well as much encouragement. Roberto Casini corrected many errors in the calculations in the preprint. H. L. also benefited from many discussions with him. Jan O. Stenflo, serving as the referee, pointed out many of our misunderstandings on the subject of scattering polarization and made many suggestions which greatly improved this paper. The infrared camera system was funded and developed in collaboration with the Michigan State University, the University of Wyoming, and Haverford College through the Astrophysical Research Consortium.

APPENDIX A

A.1. COORDINATE AND BASE VECTOR TRANSFORMATION MATRICES

The transformation of the vector components from the Cartesian coordinate system to the circular polarization coordinate system, $(A_+, A_-, A_z)^t = \epsilon(A_x, A_y, A_z)^t$ (Jefferies et al. 1989):

$$\epsilon = \frac{1}{\sqrt{2}} \begin{pmatrix} 1 & -i & 0 \\ 1 & i & 0 \\ 0 & 0 & \sqrt{2} \end{pmatrix}. \quad (\text{A1})$$

Its inverse transformation ϵ^{-1} is

$$\epsilon^{-1} = \frac{1}{\sqrt{2}} \begin{pmatrix} 1 & 1 & 0 \\ i & -i & 0 \\ 0 & 0 & \sqrt{2} \end{pmatrix}. \quad (\text{A2})$$

Using these definitions, the transformation of the base vectors from the Cartesian coordinate system to the circular polarization coordinate system for the base vectors is $(\hat{e}_+, \hat{e}_-, \hat{z})^t = \epsilon(\hat{x}, \hat{y}, \hat{z})^t$.

The coordinate transformation from the observer's coordinate system (also the scattered radiation field coordinate system) to the magnetic field coordinate system \mathbf{P} and its inverse transformation \mathbf{P}^{-1} are

$$\mathbf{P} = \mathbf{R}_y(\gamma)\mathbf{R}_z(\chi) = \begin{pmatrix} \cos \gamma & 0 & -\sin \gamma \\ 0 & 1 & 0 \\ \sin \gamma & 0 & \cos \gamma \end{pmatrix} \begin{pmatrix} \cos \chi & \sin \chi & 0 \\ -\sin \chi & \cos \chi & 0 \\ 0 & 0 & 1 \end{pmatrix}, \quad (\text{A3})$$

$$= \begin{pmatrix} \cos \gamma \cos \chi & \cos \gamma \sin \chi & -\sin \gamma \\ -\sin \chi & \cos \chi & 0 \\ \sin \gamma \cos \chi & \sin \gamma \sin \chi & \cos \gamma \end{pmatrix}; \quad (\text{A4})$$

$$\mathbf{P}^{-1} = \mathbf{R}_z(-\chi)\mathbf{R}_y(-\gamma) = \begin{pmatrix} \cos \chi & -\sin \chi & 0 \\ \sin \chi & \cos \chi & 0 \\ 0 & 0 & 1 \end{pmatrix} \begin{pmatrix} \cos \gamma & 0 & \sin \gamma \\ 0 & 1 & 0 \\ -\sin \gamma & 0 & \cos \gamma \end{pmatrix}, \quad (\text{A5})$$

$$= \begin{pmatrix} \cos \gamma \cos \chi & -\sin \chi & \sin \gamma \cos \chi \\ \cos \gamma \sin \chi & \cos \chi & \sin \gamma \sin \chi \\ -\sin \gamma & 0 & \cos \gamma \end{pmatrix}. \quad (\text{A6})$$

A.2. DERIVATION OF THE WEAK-FIELD APPROXIMATION

In the weak-field limit, the interaction matrix $N(\omega)$ can be expanded by the Taylor series expansion of ω_B ,

$$N = N(\omega) \begin{pmatrix} 1 & 0 & 0 \\ 0 & 1 & 0 \\ 0 & 0 & 1 \end{pmatrix} + N'(\omega)\omega_B \begin{pmatrix} 1 & 0 & 0 \\ 0 & -1 & 0 \\ 0 & 0 & 0 \end{pmatrix} + \frac{1}{2}N''(\omega)\omega_B^2 \begin{pmatrix} 1 & 0 & 0 \\ 0 & 1 & 0 \\ 0 & 0 & 0 \end{pmatrix} \quad (\text{A7})$$

$$= N(\omega)N^{(0)} + N'(\omega)\omega_B N^{(1)} + \frac{1}{2}N''(\omega)\omega_B^2 N^{(2)} + \dots \quad (\text{A8})$$

In this form, the frequency- and geometry-dependent parts of the interaction matrices are nicely decoupled. Since the subsequent derivation of the electric field scattering matrix involves only geometrical transformations between different coordinate systems, we will only consider the geometrical parts of the scattering function and add the frequency-dependent part of the function when we derive the Stokes vector scattering matrices.

Using the definition of the forward scattering matrix of the electric field \mathbf{H} in equation (9). We can derive

$$\mathbf{H} = N(\omega)\mathbf{H}^{(0)} + N'(\omega)\omega_B \mathbf{H}^{(1)} + \frac{1}{2}N''(\omega)\omega_B^2 \mathbf{H}^{(2)} + \dots, \quad (\text{A9})$$

with the geometry-dependent parts of the functions as

$$\mathbf{H}^{(0)} = \bar{\mathbf{r}}\mathbf{P}^{-1}\epsilon^{-1}\mathbf{N}^{(0)}\epsilon\mathbf{P} = \begin{pmatrix} 1 & 0 & 0 \\ 0 & 1 & 0 \\ 0 & 0 & 0 \end{pmatrix}; \quad (\text{A10})$$

$$\mathbf{H}^{(1)} = \bar{\mathbf{r}}\mathbf{P}^{-1}\epsilon^{-1}\mathbf{N}^{(1)}\epsilon\mathbf{P} = -i \begin{pmatrix} 0 & \cos \gamma & -\sin \gamma \sin \chi \\ -\cos \gamma & 0 & \sin \gamma \cos \chi \\ 0 & 0 & 0 \end{pmatrix}; \quad (\text{A11})$$

$$\mathbf{H}^{(2)} = \bar{\mathbf{r}}\mathbf{P}^{-1}\epsilon^{-1}\mathbf{N}^{(2)}\epsilon\mathbf{P} = \begin{pmatrix} \cos^2 \gamma \cos^2 \chi + \sin^2 \chi & -\sin^2 \gamma \cos \chi \sin \chi & -\cos \gamma \sin \gamma \cos \chi \\ -\sin^2 \gamma \cos \chi \sin \chi & \cos^2 \gamma \sin^2 \chi + \cos^2 \chi & -\cos \gamma \sin \gamma \sin \chi \\ 0 & 0 & 0 \end{pmatrix}. \quad (\text{A12})$$

Combining equations (A10)–(A12), and the transformation matrix \mathbf{R} (from eq. [31]) between the incident and scattering direction, we can derive the general electric field scattering matrix $\mathbf{M}^{(i)} \equiv \mathbf{H}^{(i)}\mathbf{R}$:

$$\mathbf{M}^{(0)} = \begin{pmatrix} 1 & 0 & 0 \\ 0 & \cos l & \sin l \\ 0 & 0 & 0 \end{pmatrix}, \quad (\text{A13})$$

$$\mathbf{M}^{(1)} = -i \begin{pmatrix} 0 & \cos l \cos \gamma + \sin \chi \sin \gamma \sin l & \cos \gamma \sin l - \sin \gamma \sin \chi \cos l \\ -\cos \gamma & -\sin \gamma \cos \chi \sin l & \sin \gamma \cos \chi \cos l \\ 0 & 0 & 0 \end{pmatrix}. \quad (\text{A14})$$

The matrix elements of the first and second row of $\mathbf{M}^{(2)}$ are

$$\begin{aligned} m_{11}^{(2)} &= \cos^2 \gamma \cos^2 \chi + \sin^2 \chi, \\ m_{12}^{(2)} &= -\sin^2 \gamma \cos \chi \sin \chi \cos l + \cos \gamma \sin \gamma \cos \chi \sin l, \\ m_{13}^{(2)} &= -\sin^2 \gamma \cos \chi \sin \chi \sin l - \cos \gamma \sin \gamma \cos \chi \cos l, \\ m_{21}^{(2)} &= -\sin^2 \gamma \cos \chi \sin \chi, \\ m_{22}^{(2)} &= (\cos^2 \gamma \sin^2 \chi + \cos^2 \chi) \cos l + \cos \gamma \sin \gamma \sin \chi \sin l, \\ m_{23}^{(2)} &= (\cos^2 \gamma \sin^2 \chi + \cos^2 \chi) \sin l - \cos \gamma \sin \gamma \sin \chi \cos l. \end{aligned} \quad (\text{A15})$$

Using Taylor's expansions of the Stokes vector scattering matrices,

$$\mathbf{S} = \mathbf{S}^{(0)} + \mathbf{S}^{(1)}\omega_B + \frac{1}{2}\mathbf{S}^{(2)}\omega_B^2 + \dots, \quad (\text{A16})$$

with

$$\mathbf{S}_0^{(0)} = N(\omega)N^*(\omega)\mathbf{S}_0[\mathbf{M}^{(0)}, \mathbf{M}^{(0)}], \quad (\text{A17})$$

$$\mathbf{S}_0^{(1)} = N(\omega)N^*(\omega)\mathbf{S}_0[\mathbf{M}^{(0)}, \mathbf{M}^{(1)}] + N'(\omega)N^*(\omega)\mathbf{S}_0[\mathbf{M}^{(1)}, \mathbf{M}^{(0)}], \quad (\text{A18})$$

$$\mathbf{S}_0^{(2)} = N(\omega)N^*(\omega)\mathbf{S}_0[\mathbf{M}^{(0)}, \mathbf{M}^{(2)}] + N''(\omega)N^*(\omega)\mathbf{S}_0[\mathbf{M}^{(2)}, \mathbf{M}^{(0)}] + 2N'(\omega)N^*(\omega)\mathbf{S}_0[\mathbf{M}^{(1)}, \mathbf{M}^{(1)}], \quad (\text{A19})$$

and the definition of $S_0(M, N)$ and $S_3(M, N)$ from equations (14) and (20):

$$S_0(M, N) \equiv \frac{1}{2} \begin{bmatrix} m_{11} n_{11}^* + m_{21} n_{21}^* + m_{12} n_{12}^* + m_{22} n_{22}^* \\ m_{11} n_{11}^* - m_{21} n_{21}^* + m_{12} n_{12}^* - m_{22} n_{22}^* \\ m_{11} n_{21}^* + m_{21} n_{11}^* + m_{12} n_{22}^* + m_{22} n_{12}^* \\ -i(m_{11} n_{21}^* - m_{21} n_{11}^* + m_{12} n_{22}^* - m_{22} n_{12}^*) \end{bmatrix}, \quad (\text{A20})$$

$$S_3(M, N) \equiv \frac{1}{2} \begin{bmatrix} m_{13} n_{13}^* + m_{23} n_{23}^* \\ m_{13} n_{13}^* - m_{23} n_{23}^* \\ m_{13} n_{23}^* + m_{23} n_{13}^* \\ -i(m_{13} n_{23}^* - m_{23} n_{13}^*) \end{bmatrix}, \quad (\text{A21})$$

we can derive the normal Stokes vectors I_0 , and the depolarizing Stokes vector I_3 to the first order of ω_B as:

$$I_0^{(0)} = \frac{1}{2} NN^* (1 + \cos^2 l), \quad (\text{A22a})$$

$$Q_0^{(0)} = \frac{1}{2} NN^* (1 - \cos^2 l), \quad (\text{A22b})$$

$$U_0^{(0)} = 0, \quad (\text{A22c})$$

$$V_0^{(0)} = 0, \quad (\text{A22d})$$

$$I_0^{(1)} = -\text{Re}(iNN'^*) \sin \gamma \cos \chi \sin l \cos l \omega_B, \quad (\text{A22e})$$

$$Q_0^{(1)} = \text{Re}(iNN'^*) \sin \gamma \cos \chi \sin l \cos l \omega_B, \quad (\text{A22f})$$

$$U_0^{(1)} = -\text{Re}(iNN'^*) [\cos \gamma (1 - \sin^2 l) - \sin \gamma \sin \chi \sin l \cos l] \omega_B, \quad (\text{A22g})$$

$$V_0^{(1)} = -\text{Im}(iNN'^*) [\cos \gamma (1 + \cos^2 l) + \sin \gamma \sin \chi \sin l \cos l] \omega_B, \quad (\text{A22h})$$

$$I_3^{(0)} = \frac{1}{2} NN^* \sin^2 l, \quad (\text{A23a})$$

$$Q_3^{(0)} = -\frac{1}{2} NN^* \sin^2 l, \quad (\text{A23b})$$

$$U_3^{(0)} = 0, \quad (\text{A23c})$$

$$V_3^{(0)} = 0, \quad (\text{A23d})$$

$$I_3^{(1)} = \text{Re}(iNN'^*) \sin \gamma \cos \chi \sin l \cos l \omega_B, \quad (\text{A23e})$$

$$Q_3^{(1)} = -\text{Re}(iNN'^*) \sin \gamma \cos \chi \sin l \cos l \omega_B, \quad (\text{A23f})$$

$$U_3^{(1)} = \text{Re}(iNN'^*) (\cos \gamma \sin^2 l - \sin \gamma \sin \chi \sin l \cos l) \omega_B, \quad (\text{A23g})$$

$$V_3^{(1)} = -\text{Im}(iNN'^*) (\cos \gamma \sin^2 l - \sin \gamma \sin \chi \sin l \cos l) \omega_B. \quad (\text{A23h})$$

The second-order terms have complicated geometrical dependence and are important only for the limb prominence observations when the scattering angle $l = 90^\circ$. We will derive the second-order terms in the next section when we discuss the prominence Hanle effect.

Using the simplified expression of $N(\omega)$ from equation (33),

$$N(\omega) = \frac{e\omega_0}{2m} \frac{1}{(\omega_0 - \omega) - i\Gamma/2}, \quad (\text{A24})$$

we can derive the frequency-dependent functions of the Stokes vector:

$$NN^* = \left(\frac{e\omega_0}{2m} \right)^2 \frac{1}{(\omega_0 - \omega)^2 + (\Gamma/2)^2}, \quad (\text{A25})$$

$$iNN'^* = \left(\frac{e\omega_0}{2m} \right)^2 \frac{i(\omega_0 - \omega) + \Gamma/2}{[(\omega_0 - \omega)^2 + (\Gamma/2)^2]^2}. \quad (\text{A26})$$

In terms of the three components of ω_B ,

$$\omega_{Bx} = \omega_B \sin \gamma \cos \chi, \quad (\text{A27})$$

$$\omega_{By} = \omega_B \sin \gamma \sin \chi, \quad (\text{A28})$$

$$\omega_{Bz} = \omega_B \cos \gamma, \quad (\text{A29})$$

and applying the Doppler broadening effect, we can rewrite equations (A22)–(A23) as

$$I_0 = h(a, v)(1 + \cos^2 l) - k(a, v)\omega_{Bx} \sin l \cos l \quad (\text{A30a})$$

$$Q_0 = h(a, v)(1 - \cos^2 l) + k(a, v)\omega_{Bx} \sin l \cos l \quad (\text{A30b})$$

$$U_0 = -k(a, v)[\omega_{Bz}(1 - \cos^2 l) - \omega_{By} \sin l \cos l] \quad (\text{A30c})$$

$$V_0 = -f(a, v)[\omega_{Bz}(1 + \cos^2 l) + \omega_{By} \sin l \cos l] \quad (\text{A30d})$$

$$I_3 = h(a, v) \sin^2 l + k(a, v)\omega_{Bx} \sin l \cos l, \quad (\text{A30e})$$

$$Q_3 = -h(a, v) \sin^2 l - k(a, v)\omega_{Bx} \sin l \cos l, \quad (\text{A30f})$$

$$U_3 = k(a, v)(\omega_{Bz} \sin^2 l - \omega_{By} \sin l \cos l), \quad (\text{A30g})$$

$$V_3 = -f(a, v)(\omega_{Bz} \sin^2 l - \omega_{By} \sin l \cos l). \quad (\text{A30h})$$

This is a significant simplification comparing the full scattering matrix of equations (13) and (14) in the main text, in which the frequency- and geometry-dependent parts of the scattering function are coupled and the geometrical dependence of the polarization signals is difficult to visualize.

A.3. PROMINENCE HANLE EFFECTS

In prominence observations $l = 90^\circ$, the first-order term in $I^{(1)}$ and $Q^{(1)}$ vanish, and the Stokes profiles in equation (A30) reduce to

$$I_0 = h(a, v), \quad (\text{A31a})$$

$$Q_0 = h(a, v), \quad (\text{A31b})$$

$$U_0 = -k(a, v)\omega_{Bz}, \quad (\text{A31c})$$

$$V_0 = -f(a, v)\omega_{Bz}. \quad (\text{A31d})$$

Thus, it is necessary to include the second-order effects for the Stokes I and Q profiles in this calculation. We will not include the second-order terms for the Stokes U and V profiles since the first-order effects should dominate these two profiles. To calculate the second-order terms, we set $l = 90^\circ$, and the electric field scattering matrices (eq. [A13]–[A15]) reduce to

$$\mathbf{M}^{(0)} = \begin{pmatrix} 1 & 0 & 0 \\ 0 & 0 & 0 \\ 0 & 0 & 0 \end{pmatrix}, \quad (\text{A32})$$

$$\mathbf{M}^{(1)} = -i \begin{pmatrix} 0 & \sin \gamma \sin \chi & \cos \gamma \\ -\cos \gamma & -\sin \gamma \cos \chi & 0 \\ 0 & 0 & 0 \end{pmatrix}, \quad (\text{A33})$$

$$\mathbf{M}^{(2)} = \begin{pmatrix} \cos^2 \gamma \cos^2 \chi + \sin^2 \chi & \cos \gamma \sin \gamma \cos \chi & -\sin^2 \gamma \cos \chi \sin \chi \\ -\sin^2 \gamma \cos \chi \sin \chi & \cos \gamma \sin \gamma \sin \chi & \cos^2 \gamma \sin^2 \chi + \cos^2 \chi \\ 0 & 0 & 0 \end{pmatrix} \quad (\text{A34})$$

From equation (17), the second-order effects consist of two terms with different frequency-dependent functions. The frequency-dependent function of the term $\mathcal{S}[\mathbf{M}^{(1)}, \mathbf{M}^{(1)}]$ is $N'N'^*$. Its contribution to the Stokes I and Q profiles are

$$I_0^{(2)} = \frac{N'N'^*}{2} \omega_B^2, \quad (\text{A35a})$$

$$Q_0^{(2)} = \frac{N'N'^*}{2} [-\cos^2 \gamma + \sin^2 \gamma (\sin^2 \chi - \cos^2 \chi)] \omega_B^2. \quad (\text{A35b})$$

The frequency-dependent function of $\mathcal{S}_0[\mathbf{M}^{(0)}, \mathbf{M}^{(2)}] + \mathcal{S}_0[\mathbf{M}^{(2)}, \mathbf{M}^{(0)}]$ is NN'^* . Its contribution to the Stokes I and Q profiles are

$$I_0^{(2)} = \frac{1}{2} \text{Re} (NN'^*) (\cos^2 \gamma \cos^2 \chi + \sin^2 \chi) \omega_B^2, \quad (\text{A36a})$$

$$Q_0^{(2)} = \frac{1}{2} \text{Re} (NN'^*) (\cos^2 \gamma \cos^2 \chi + \sin^2 \chi) \omega_B^2. \quad (\text{A36b})$$

Notice that the right-hand side of equations (A36a) and (A36b) are identical. Thus, the second-order terms in the Stokes Q profile which depend on the function NN'^* do not change the degree of polarization of the Stokes Q signal, and we will ignore it in the rest of the discussion.

The explicit form of $N'N'^*$ is

$$\begin{aligned} N'N'^* &= \left(\frac{e\omega_0}{2m} \right)^2 \frac{1}{[(\omega_0 - \omega)^2 + (\Gamma/2)^2]^2}, \\ &= \frac{2}{\Gamma} \operatorname{Re} (iNN'^*). \end{aligned} \quad (\text{A37})$$

Using the definition of the Doppler broadened profiles in equations (39)–(41) and the definition of $\omega_{B(x,y,z)}$ in equations (A27)–(A29), we can write the Stokes profiles of the prominence Hanle effect as

$$I_0 = h(a, v) + \frac{1}{\Gamma} k(a, v)\omega_B^2, \quad (\text{A38a})$$

$$Q_0 = h(a, v) - \frac{1}{\Gamma} k(a, v)\omega_B^2 [\cos^2 \gamma + \sin^2 \gamma (\cos^2 \chi - \sin^2 \chi)], \quad (\text{A38b})$$

$$U_0 = -k(a, v) \cos \gamma \omega_B, \quad (\text{A38c})$$

$$V_0 = -f(a, v) \cos \gamma \omega_B. \quad (\text{A38d})$$

REFERENCES

- Anzer, U., & Tandberg-Hanssen, E. 1970, *Sol. Phys.*, 11, 61
 Babcock, H. D., & Babcock, H. W. 1955, *ApJ*, 121, 349
 Bommier, V. 1978, in *IAU Colloq. 44, Physics of Solar Prominence*, ed. E. Jensen, P. Maltby & F. Q. Orral (Oslo: Institute of Theoretical Physics), 93
 Bommier, V., Landi Degl'innocenti, E., Leroy, J. L., & Sahal-Br  chot, S. 1994, *Sol. Phys.*, 154, 231
 Bommier, V., Leroy, J. L., & Sahal-Br  chot, S. 1981, *A&A*, 100, 231
 Chang, E. S., & Deming, D. 1997, *BAAS*, 29, 906
 Chou, Y. P., & Low, B. C. 1994, *Sol. Phys.*, 153, 255
 De Jager, C., Namba, O., & Neven, L. 1966, *Bull. Astron. Inst. Netherlands*, 18, 128
 Hirayama, T. 1971, *Sol. Phys.*, 17, 50
 House, L. L. 1971, in *IAU Symp. 43, Solar Magnetic Fields*, ed. R. Howard (Boston: Reidel), 130
 Jackson, J. D. 1975, *Classical Electrodynamics* (New York: Wiley)
 Jefferies, J., Lites, B. W., & Skumanich, A. 1989, *ApJ*, 343, 920
 Kippenhahn, R., & Schl  ter, A. 1957, *Z. Astrophys.*, 43, 36
 Kuhn, J. R., Balasubramaniam, K., Kopp, G., Penn, M. J., Dombard, A. J., & Lin, H. 1994, *Sol. Phys.*, 153, 143
 Kuperus, M., & Raadu, M. A. 1974, *A&A*, 31, 189
 Landi Degl'innocenti, E. 1982, *Sol. Phys.*, 79, 291
 Leroy, J. L. 1989, in *Dynamics and Structure of Quiescent Solar Prominences*, ed. E. R. Priest (Dordrecht: Kluwer), 77
 Leroy, J. L., Bommier, V., & Sahal-Br  chot, S. 1984, *A&A*, 131, 33
 Lin, H. 1995, *ApJ*, 446, 421
 Martin, S. F., Bilimoria, R., & Tracadas, P. W. 1994, in *NATO ASI Ser., Vol. 443, Solar Surface Magnetism*, ed. R. J. Rutten & C. J. Schrijver (Dordrecht: Kluwer), 303
 Martin, S. F., & Echols, C. R. 1994, in *NATO ASI Ser., Vol. 443, Solar Surface Magnetism*, ed. R. J. Rutten & C. J. Schrijver (Dordrecht: Kluwer), 339
 Mihalas, D. 1978, *Stellar Atmospheres* (New York: Freeman)
 Milkey, R. W., Heasley, J. N., & Beebe, H. A. 1973, *ApJ*, 186, 1043
 Rust, D. M., & Kumar, A. 1994, *Sol. Phys.*, 155, 69
 Sakurai, T. 1989, *Space Sci. Rev.*, 51, 1
 Stenflo, J. O. 1982, *Sol. Phys.*, 80, 209
 ———. 1994, *Solar Magnetic Fields, Polarized Radiation Diagnostics* (Dordrecht: Kluwer)
 Tandberg-Hanssen, E. 1974, *Solar Prominences* (Dordrecht: Reidel)
 Zirin, H. 1975, *ApJ*, 121, 349